

Ensembles in Urban Large Eddy Simulations with Changing Wind Direction

Jukka-Pekka Keskinen and Antti Hellsten

Finnish Meteorological Institute, Helsinki, Finland

January 14, 2025

Abstract

Differences between time-averaged and ensemble-averaged wind are studied in this article for the case of changing wind direction. We consider a flow driven by a temporally turning pressure gradient in both an idealized case of a staggered cube array and a realistic urban environment. The repeating structure of the idealized case allows us to construct a large ensemble of 3 240 members with a reasonable compute time. The results indicate that the use of plain time average instead of an ensemble average allows for accurate calculation of only the along-wind mean velocity. Utilising Taylor diagrams, we show that a reasonable compromise between ensemble size and accuracy can be achieved utilising a 30-minute time average together with a 50-member ensemble for the flow within the urban roughness sublayer. During this 30-minute averaging period, the wind direction turns for approximately 4.8° . By applying this approach to the realistic urban geometry, we identify building wakes as the regions most severely affected by the incorrectly utilized time averaging.

1 Introduction

Cities and other urban areas are an important environment for the majority of the world's population. The wind flow through the city, in turn, has a large impact on the health and comfort of the people living in the city. The wind affects the urban air quality by transporting and mixing pollutants, emitted within the city or at some upstream location. The air flow through the city can also mitigate the urban heat island effect by removing excess heat. On the other hand, strong winds within the street level can be perceived as uncomfortable by the inhabitants. It is hence important to understand the details of the flow in and around cities.

Large eddy simulation (LES) is an approach for the numerical solution of fluid flows (see e.g. Pope (2000)). It based on the idea of resolving the major turbulent motions while utilising parametrisations for the minor features. LES

provides an excellent compromise between accuracy and computational costs. It has been applied in a wide variety of different topics, ranging from clouds (Ahola et al. 2022) to engine parts (Keskinen et al. 2011). In the future, the continual increase in available computational power will make LES an attractive option for an even wider variety of flows.

LES has been used successfully to simulate the flow and dispersion in cities and city-like geometries for more than 15 years (Hanna et al. 2006; Tseng et al. 2006; Letzel et al. 2008; Karttunen et al. 2020; Giometto et al. 2017; Park et al. 2015; Letzel et al. 2012). LES is very suitable for the task as it resolves a large part of the turbulence of the flow and can thus be used to study the intermittent interaction between the wind and the buildings. Unlike experimental approaches, LES also allows one to access the three-dimensional, time-dependant flow field and thus provides a more comprehensive view on the wind field.

Due to the time-resolved nature of LES, it is well suited for the simulation of transient flows. In the context of urban flows, transient aspects can enter the simulation, for example, through the use of dynamic boundary conditions (Kurppa et al. 2020; Lin et al. 2021; Park et al. 2015). The dynamic boundary conditions enter the LES often through coupling to a meso-scale numerical weather prediction model. These types of simulations are expected to become more numerous in the future and have been designated as an answer to a Grand Challenge in environmental fluid mechanics (Dauxois et al. 2021).

Transient flows are not statistically stationary and hence plain time averaging is not a valid approach anymore. This introduces additional difficulties in the interpretation of the output data. In earlier studies on transient urban flows, statistical values have been calculated mostly using short time averages (from 1 minute to 1 hour) (Khan et al. 2021; Park et al. 2015; Lin et al. 2021), spatial averaging in the horizontal direction (Kurppa et al. 2020; Lin et al. 2021), or as a combination of both (Park et al. 2015; Kurppa et al. 2020). The use of short time averages implies an assumption on the approximate statistical stationary during the averaging time. The use of horizontal averaging, on the other hand, is strictly appropriate only if the flow is homogeneous in the horizontal direction.

In order to obtain reliable statistical quantities from a transient flow, ensemble averaging is required. An ensemble can be created by performing a set of transient simulations that are somehow perturbed, for example by starting them with different initial conditions. However, one must keep in mind that the perturbations should not modify the statistics of the simulations. Ensemble averaging is widely used in numerical weather prediction (Leutbecher and Palmer 2008) and climate modelling (Eyring et al. 2016). In the context of atmospheric LES, ensemble approaches are less common but have been utilized previously to study different topics including forest edge flow (Kanani et al. 2014), flow past an isolated hill (Chow and Street 2009), and the convective boundary layer (Maronga and Raasch 2013).

The authors of this article are aware of only three other publications reporting LES ensembles in urban or urban-like environments. In the earliest one, Patnaik et al. (2007) studied the dispersion of a contaminant in Downtown Los Angeles, USA, using an eight-member LES ensemble and compared it against

field measurements. Comparison against the measurements was carried out using statistical approaches as each release of the experiments was considered a single realisation of the same dispersion case. The variation between the ensemble members appeared large and the authors associate this with the vortex shedding by the buildings.

A larger LES ensemble of 60 members was created together with corresponding wind tunnel measurements by Harms et al. (2011) for studying the dispersion of puffs in the Central Business District in Oklahoma City, USA. Based on the experiments, an ensemble of at least 200 members is required for statistically reliable results with a dependency on the distance to release point. The authors performed a statistical comparison between the experiments and the simulations based on the peak time of the puffs for two measurement locations. The comparison resulted in conflicting performance of the simulations against the measurements, which was attributed to both strong spatial variation of the flow and the suitability of the quantity used in the comparison.

More recently, Li and Giometto (2023) considered an idealized urban flow consisting of cube-array driven by a pulsatile forcing. The periodic nature of the forcing allows for accumulating sufficient statistics during a single simulation and, depending on the frequency of the forcing, averaging was done over 80–1000 forcing cycles. Together with spatial averaging over the 192 repeating units of the cube-array, Li and Giometto (2023) performed their analysis using ensembles with 15 360–192 000 members. They observed that the flow unsteadiness had a significant effect on the time-averaged statistics although some quantities, such as roughness height and shear stress, were not affected.

The reason for the lack of further urban LES ensembles, especially on real urban areas, is clear: computational cost. In order to capture the interaction between the flow and the buildings, a resolution down to the order of metres is required. On the other hand, cities are large entities so that the computations have to be made with grids containing tens or hundreds of millions grid points. Performing some tens of simulations with these requirements is a formidable task but might not be enough as a sufficient ensemble size was estimated to be 200 members in the case of Oklahoma (Harms et al. 2011). Properly converged higher-order statistics might require even more members, perhaps something similar to the 15 360–192 000 member ensembles of Li and Giometto (2023).

It is obvious that transient urban flows will be studied using LES in the future and it is expected that many of these studies will be done without a sufficiently large ensemble. The use of time averages will allow these studies to provide useful information but it is unclear how reliable this kind of averaging is in the case of transient flows. The accuracy of this approach is questionable especially when one is considering the flow in the roughness sublayer, in close vicinity to buildings and other obstacles. It is thus important to estimate how accurately one can study urban flows and especially the flow within the roughness sublayer. Furthermore, as the computational resources available to LES are constantly increasing and ensembles become more accessible, it is important to obtain an estimate for a sufficient ensemble size for urban LES.

In this article we study the difference between time averaging and ensemble

averaging in the case of urban flows with non-stationary forcing as well as the requirements for the number of ensemble members. We consider two cases: an idealized case of cube array in staggered formation and a real city. In both cases, a rotating pressure gradient is used to drive the flow. By comparing time-averaged and ensemble-averaged quantities, we observe clear differences especially when fluctuating velocities are concerned. Based on the spread of the ensemble members, we give an estimate for the ensemble size for reliable LES in the case of urban flows. The numerical approaches, including the ensemble averaging approach, are described next in Section 2. The results are given then in Section 3, followed by the conclusions in Section 4.

2 Numerical Methods

We utilized the PALM model to simulate the flow past a cube array and a real urban environment. Details of the applied LES approach are given in section 2.1 and a description of the used model can be found from section 2.2. The set-up of the flow including the details of the cube array and the urban environment are given in section 2.3 while the details of the applied ensemble approach are described in section 2.4.

2.1 Large Eddy Simulation

In LES, the large scale motions of the flow are solved while the smaller scales, the subgrid scales (SGS), are left unsolved and their effects on the large scales are parameterized. Formally this scale separation is achieved by a filtering operation. In most cases, including the present work, the filtering is carried out implicitly by the computational grid.

In the case of an incompressible flow at a very high Reynolds number, the filtered continuity equation and the filtered Navier-Stokes equations are

$$\begin{aligned} \frac{\partial \bar{u}_j}{\partial x_j} &= 0, \quad \text{and} \\ \frac{\partial \bar{u}_i}{\partial t} &= -\bar{u}_j \frac{\partial \bar{u}_i}{\partial x_j} - \frac{\partial \bar{p}}{\partial x_i} - \frac{\partial \tau_{ij}^r}{\partial x_j} - \bar{f}_i, \end{aligned}$$

where x_i is the position, t is time, u_i is the fluid velocity, p is the modified perturbation pressure divided by density, and f_i contains all body forces acting on the fluid. The filtered quantities are indicated using the overbar while the lower index denotes the coordinate direction in a three-dimensional Cartesian coordinate system with a repeated index within a term implying summation over the coordinate directions according the Einstein summation convention. The effects of SGS on the resolved scales are represented through the anisotropic residual stress tensor τ_{ij}^r . The isotropic part of the residual stress tensor is included in the modified perturbation pressure.

The SGS can be parametrized using a variety of different approaches. In atmospheric LES, Deardorff's 1.5-order parametrisation (Deardorff 1980; Sagaut

2006) is a common choice and we apply it according to the implementation of Maronga et al. (2015). The parametrisation is of the eddy-viscosity type where

$$\tau_{ij}^r = -K_m \left(\frac{\partial \bar{u}_i}{\partial x_j} + \frac{\partial \bar{u}_j}{\partial x_i} \right)$$

and the SGS eddy diffusivity is given as

$$K_m = c_m l \sqrt{e}$$

with the model constant $c_m = 0.1$, the SGS mixing length l , and the SGS turbulent kinetic energy e . In the case of neutral stratification $l = \min(1.8z, \Delta)$, where z is the distance from the bottom wall and $\Delta = \sqrt[3]{\Delta x_1 \Delta x_2 \Delta x_3}$ characterizes the local grid spacing using the actual grid spacings Δx_i for all coordinate directions. The SGS turbulent kinetic energy is obtained by solving an additional transport equation:

$$\frac{\partial e}{\partial t} = -\bar{u}_j \frac{\partial e}{\partial x_j} - \tau_{ij}^r \frac{\partial \bar{u}_i}{\partial x_j} - \frac{\partial \gamma_j}{\partial x_j} - \epsilon,$$

where the turbulent diffusion term is parametrized using the gradient hypothesis with

$$\gamma_j = -2K_m \frac{\partial e}{\partial x_j}$$

and the turbulent dissipation term by using

$$\epsilon = \left(0.19 + 0.74 \frac{l}{\Delta} \right) \frac{e^{3/2}}{l}.$$

2.2 Computational Set-Up

In this study, we use the PALM model system, version 6.0 (Maronga et al. 2020, 2015). It is a highly parallelisable code that has been utilized for more than 20 years, mainly for the simulation of various atmospheric boundary layer flows. The model can be used to perform both LES and Reynolds-Averaged Navier-Stokes simulations. In order to take consider the effects of buoyancy, the Boussinesq or the anelastic approximations can be used. PALM contains a variety of model components allowing one to consider the effects due to e.g. radiation and microphysics.

We use PALM to carry out LES and solve the filtered, incompressible Navier-Stokes equations at a very high Reynolds number. The equations are solved using finite differences with the fifth order upwind-biased numerical scheme by Wicker and Skamarock (2002) for the advective terms and the third-order Runge-Kutta method by Williamson (1980) for time advancement. To ensure the incompressibility of the flow field, a predictor-corrector method is utilized in PALM. Divergences in the initial flow field are attributed solely to the pressure term and the resulting Poisson equation for the modified perturbation pressure

is solved after each Runge-Kutta step (see e.g. Patrinos and Kistler (1977)) using an iterative multi-grid scheme (see e.g. Hackbusch (1985)). PALM is parallelized with MPI (Gropp et al. 1999) and using a two-dimensional domain decomposition in the horizontal directions.

The computations are carried out on the Puhti supercomputer provided by CSC – IT Center for Science Ltd. Puhti is an Atos Bullsequana X400 platform with each node containing two Intel Xeon processor (Cascade Lake) with 20 cores each at 2.1 GHz.

2.3 Case Set-Up

We have simulated two different flows: a flow past a staggered cube array and flow past a realistic urban environment. The cube array is computationally relatively inexpensive, allowing us to obtain a large number of ensemble members. Although the cube array can be viewed as an idealized urban environment, real cities very rarely have such a high level of regularity. For this reason we also study the flow past the city of Turku, Finland.

2.3.1 Staggered Cube Array

We investigate the flow past an array of 648 cubes with edge length of h arranged in a staggered formation in the x direction and lined up in the y direction. The distance between the cubes in both x and y direction is h . The arrangement in the horizontal (xy) plane is shown in Fig. 1. It contains a repeating pattern with one cube and adjoining empty space, denoted in the figure with a dashed line. The size of the domain is $72h$ in the x direction, which is also the main flow direction. In the y direction the domain spans $36h$ and in the vertical (z) direction the domain is $6h$. The size of the computational domain was chosen according to the recommendations by Munters et al. (2016). The array can be characterized using the plan area index λ_p , defined as the horizontal area of the cubes divided by the horizontal area of the domain, and the frontal area index λ_f , defined as the windward area of the cubes divided by the horizontal area of the domain. In the current case of a regular array of cubes, we have $\lambda_p = \lambda_f = \frac{1}{4}$ with no variation with the wind direction. Flows with similar staggered cube arrays have been studied extensively in the past, both numerically (e.g. Leonardi and Castro (2010); Cheng and Porté-Agel (2015); Ahn et al. (2013)) and experimentally (e.g. Blackman et al. (2015); Hagishima et al. (2009)).

The simulations on the staggered cube array were carried out using an equidistant mesh with 1152 grid points in the x direction, 578 grid points in the y direction, and 96 grid points in the z direction. This resulted in approximately 64 million grid points in total. The mesh resolves each obstacle with 16 grid points in each direction, conforming with the recommendations of Xie and Castro (2006). We have set $h = 32$ m and hence the grid spacing is 2 metres.

All lateral boundaries are cyclic. However, during initial tests with a smaller cube array we observed very large streamwise structures in the flow when the pressure gradient was directed along the x axis. For this reason, we have applied

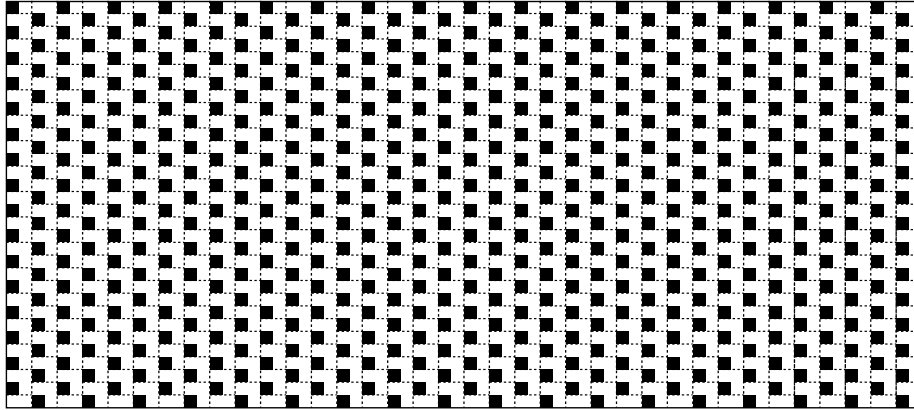


Figure 1: Staggered cube array as viewed from top. All cubes are the same size width and separation. The repeating pattern consisting of a cube and adjoining empty space is used in calculating averages and is denoted for each cube using dashed line. On every second column the repeating pattern is wrapped from top to bottom due to cyclic boundary conditions. The full extent of the computational domain is shown with a solid line

a shift of one repeating unit in the y direction between the yz domain boundaries in order to remove these structures (Munters et al. 2016). At the upper boundary, we applied the zero-gradient boundary condition while the lower boundary was set to no-slip. The flow was driven using a pressure gradient with a constant magnitude of $0.0008 \text{ m}^2 \text{ s}^{-2}$.

First, a spinup simulation was carried out. The direction of the pressure gradient was kept constant with wind from 240° . The turbulence was allowed to develop for 18 hours after which the flow was considered fully developed. Simulations with a turning pressure gradient were branched off from the spinup. The turning speed of the pressure gradient was constant at $\Omega = 15^\circ \text{ h}^{-1} \approx 7.3 \times 10^{-5} \text{ s}^{-1}$ and hence at the end of the four hour simulation, the pressure gradient was directed at 300° . The nondimensional number characterising the flow with a turning pressure gradient is the (modified) Rossby number $Ro = U_b / (H\Omega) \approx 210$, where $H = 194 \text{ m}$ is the domain height and $U_b = 2.9 \text{ ms}^{-1}$ is the bulk velocity of the flow.

2.3.2 Realistic Urban Environment

In addition to the cube array, we study also a flow past a real urban environment. The considered urban area is the city of Turku, located in southwestern Finland, on the coast of the Baltic sea. The terrain in Turku is relatively flat: its height ranges from zero at sea level to approximately 55 meters. We concentrate on Turku's Student village, a residential area located just outside central Turku and characterized by low-rise buildings, houses, and trees. The same area has

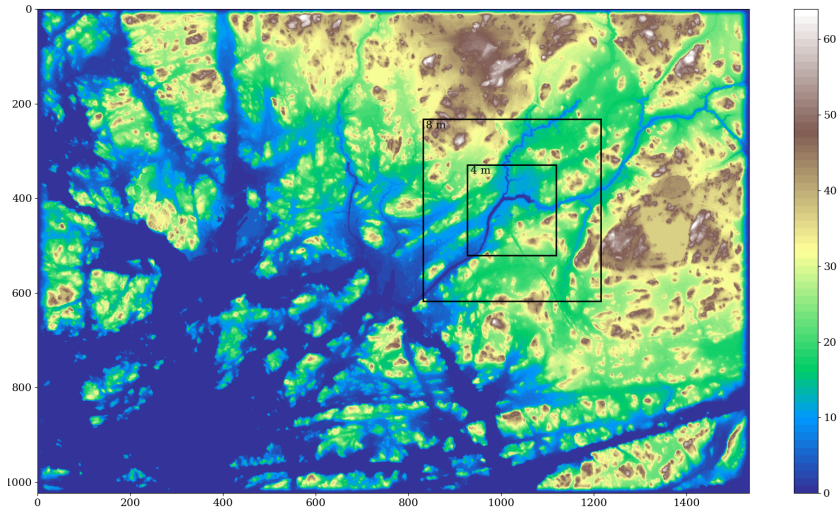


Figure 2: Terrain height (m) in the simulated area. The intermediate and the small domain are indicated on the figure with black squares. The Student village is located at the centre of the smallest domain, south from the river. North is up

been studied earlier with a similar computational setup by Keskinen et al. (in press) for the dispersion of a passive scalar.

For most parts, we have set up our simulations using height information from existing LIDAR data, provided by the city of Turku. These data provide height information separately for terrain, buildings, and vegetation. For those areas that extend beyond the borders of the city of Turku, the digital terrain model of the National Land Survey of Finland was used. We also added two buildings that were constructed after the collection of the LIDAR data using vector files provided by the city of Turku. An overview of the simulated area is given using terrain height in Fig. 2.

Our simulations are carried out using three, two-way coupled computational domains that are nested within each other and with increasing resolution using PALM’s nesting feature (Hellsten et al. 2021). The largest domain spans approximately $25 \text{ km} \times 16 \text{ km} \times 670 \text{ m}$, the intermediate domain $6 \text{ km} \times 6 \text{ km} \times 260 \text{ m}$, and the smallest domain $3 \text{ km} \times 3 \text{ km} \times 190 \text{ m}$. The largest domain has 1536×1024 grid points in the horizontal directions with grid spacing of 16 metres. The two inner domains have 768×768 grid points with a spacing of 8 metres in the intermediate domain and 4 metres in the smallest domain. In the vertical direction, the largest domain has 64 grid points with the grid spacing varying from 8 metres close to the ground to 16 metres at the domain top. The intermediate and the small domain have 64 and 96 equally spaced grid points in the vertical direction with grid spacings of 4 metres and 2 metres. The domains are marked using black lines in Fig. 2. Our main interest is in the innermost

domain. For this reason, some simplifying modelling choices have been made in the description of the outermost domain. Firstly, only the orographical features are accounted for in the outermost domain i.e. buildings and vegetation are not considered. Secondly, we apply cyclic boundary conditions on the lateral boundaries. In order to facilitate this, the orography has been forced to zero at the boundaries by creating a slope. Thirdly, an irregular array of elongated porous objects have been placed on the uppermost part of the domain in order to break up unphysical persistent large-scale flow structures maintained by the cyclic boundary conditions and thus to reduce the time required to achieve a statistically steady flow. On the lower boundary, the rough-wall boundary condition based on the Monin–Obukhov similarity theory is used (Maronga et al. 2020), while the slip condition is utilized on the upper boundary.

In the inner domains, a higher level of detail is applied. Solid obstacles, such as orography and buildings, are resolved using the masking method as described by Maronga et al. (2015). Trees and other vegetation are treated as porous objects (momentum sinks). The inner domains obtain their lateral and top boundary conditions from the larger domain they are nested in. The two-way coupling of the nested domains is active at height above 150 meters. The lower boundary is considered as a rough-wall similarly to outermost domain.

In the same manner as with the cube array, the flow was driven using a pressure gradient with a constant magnitude of $5.0 \times 10^{-3} \text{ m}^2\text{s}^{-2}$ and directed at 240° . The body force is applied in the upper parts of the outermost domain, above 350 metres. The resulting flow has a bulk velocity $u_b \approx 10.5 \text{ ms}^{-1}$, calculated using the mean horizontal wind speed in the largest domain. We performed simulations both with stationary and turning pressure gradients. In the latter case, we tried to match the conditions of the cube array and used the same turning speed: $\Omega = \pm 15^\circ\text{h}^{-1} \approx 7.3 \times 10^{-5} \text{ s}^{-1}$. The temporal extent of the simulation was also the same four hours and the pressure gradient was pointing at 300° at the end of the simulation. The nondimensional number characterising the flow with a turning pressure gradient is the (modified) Rossby number $Ro = U_b/(H\Omega) \approx 210$, calculated using values for the largest domain as this is where the turning pressure gradient is applied.

The simulations are started by initialising a laminar flow state with an approximately realistic wind profile in the largest domain. The flow is then allowed to adjust and develop large scale turbulence for eight hours without the smaller domains. After this first spinup simulation, a second eight-hour spinup is performed with two-way coupling enabled in order to properly initialize the inner domains with fully developed turbulence. The final simulations are then carried out with the turning pressure gradient, branching off from the spinup.

2.4 Ensemble Approach

We have created our ensembles of turning pressure gradient simulations by branching from a fully developed, constant pressure gradient simulation. In other words, we sample full flow fields from the constant pressure gradient simulation at fixed time intervals and then use these as initial conditions in the

simulations with a turning pressure gradient. This approach is used in climate modelling and it was indicated as a “common way to do” ensembles in the sixth coupled climate model comparison project (CMIP6) (Eyring et al. 2016).

The sampled initial conditions should possess a representative amount of variation. In the case of turbulent flow this means that one should not sample the flow with intervals smaller than the integral time scale. Furthermore, in many cases the flow possesses structures that are much larger than the integral scale and one should aim at capturing the full variability of the flow by sampling beyond these scales.

We have chosen to sample the constant pressure gradient flow with 20 minute intervals. In the case of the cube array, this is approximately 1.5 times the flow-through-time and should be enough to make each realisation independent. In the case of cube array, we also exploit the repeating pattern by averaging over each as if they were a separate ensemble members. Some spatial correlation of samples is expected to enter the ensemble due to this. We assume that the time separation between the initial condition should mitigate the effect of using the repeating pattern in the ensemble calculation. In the case of the realistic urban environment, 20 minutes is approximately two flow-through times in the smallest domain and approximately half a flow-through time in the largest domain.

3 Results

Simulation ensembles were created for both the staggered cube array and for the realistic urban environment using the approaches described earlier. In both cases, we concentrate at the time instant in the middle of the simulation, at two hours since the start of the turning of the pressure gradient. Any time averaging is hence centred around $t = 120$ min and, for example, the 30 minute time average has been calculated with $t = [105, 135]$ min.

3.1 Staggered cube array

Using the staggered cube array setup, we have carried out a 19 hours and 20 minutes long spinup simulation with a static pressure gradient. The kinetic energy content of the spinup is shown in Fig.3 a) using black colour. The initial development from zero is quick and the flow reaches its final energy level already after approximately three simulated hours. After this, the flow assumes relatively steady energy level with minor fluctuations. We monitored the velocity profiles and allowed the turbulence to develop for 15 more hours.

Starting at 18 hours, five simulations with a turning pressure gradient are branched off every 20 minutes from the spinup and simulated for four hours. The introduction of the turning pressure gradient alters the kinetic energy content with all runs showing a maximum after 1.5–2.5 hours after the start of pressure gradient turning, as seen in Fig.3 b). Otherwise the kinetic energy content develops differently in all simulation although the level of fluctuation is still

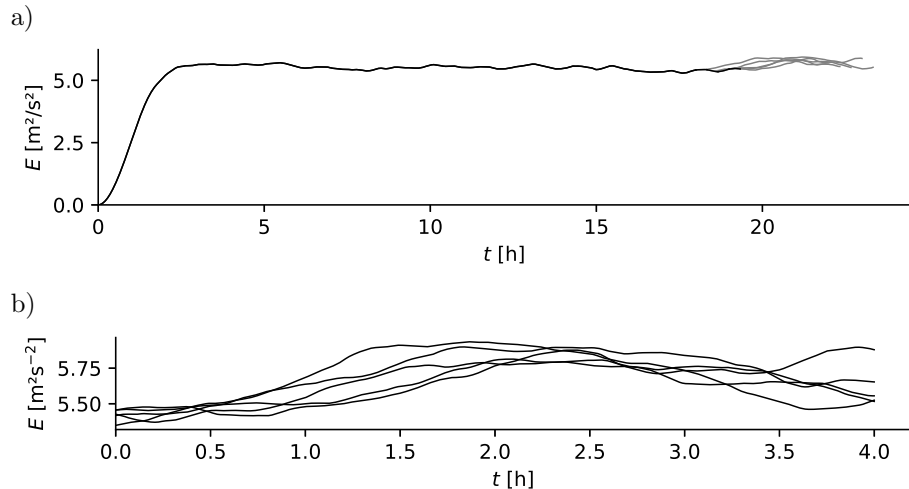


Figure 3: Resolved kinetic energy content of the simulations with the staggered cube array. a) The spinup simulation (black) and the simulations with a turning pressure gradient (grey). The turning pressure gradient simulations branch off from the spinup every 20 minutes starting at 18 hours since the beginning of the spinup. b) All turning pressure gradient simulations shown using time since start of pressure gradient turning

similar. The spinup simulation required approximately 5 000 core hours while each run consumed approximately 1 000 core hours on average.

The mean wind direction (not shown), calculated using only the upper parts of the domain, is approximately 241° at the beginning of the simulation. It follows the approximate direction of the pressure gradient with a lag. The wind turning appears to happen in two parts: a fast acceleration during the first 40 minutes of the simulation up to approximately 8°h^{-1} and somewhat slower acceleration during the rest of the simulation up to approximately 14°h^{-1} . The mean wind direction at middle of the simulation is approximately 257° and 282° at the end of the simulation.

The staggered cube array has 648 repeating units and hence the total ensemble size is 3 240 when we count both simulations and the repeating units. Using all ensemble members together with averaging in the horizontal direction we obtain vertical profiles of the ensemble mean velocities and variances shown with a black line in Fig. 4. The profiles indicate a typical flow over cubical obstacles with highest mean velocities at the top and a maxima for variances at the cube height. The 25th and 75th percentile of the ensemble members are indicated by two thinner blue lines. Their separation, the interquartile range, quantifies the variation within an ensemble (Harman et al. 2016).

The effect of time averaging on the mean velocity profiles is shown in Fig. 4 a)–c) using 25th and 75th percentiles for a short (10 minute), medium (30

minute), and long (210 minute) time-averages. These correspond approximately to 0.92° , 4.8° , and 37° change in wind direction, respectively. For mean velocities, the use of both the short and the medium averaging time narrows the interquartile range around the ensemble mean for all components. However, the longer averaging time results in a narrow interquartile range that's away from the ensemble mean for the u and v components of the velocity. This can be explained by the relatively large change in the overall wind direction during the time-averaging, caused by the turning pressure gradient.

In the case of velocity variances, shown in Fig. 4 d)–f), the effect of time averaging is detrimental almost always. The ensemble mean variance lies within the interquartile range only for short times and only within the roughness sublayer. The most extreme case is seen for long time average in σ_y^2 . In all cases, the time-averaged variances are larger than the true, ensemble averaged variances. This indicates that a part of the change in mean wind ends up in the variances.

Further insight in to the flow field within in the close vicinity of the obstacles is obtained from Fig. 5 and 6 where planes cutting the repeating element are shown. The mean velocity components in panels a)–c) of both figures reveal that the main flow direction is toward positive x . Recirculation regions in the vertical direction can be seen on all vertical sides of the obstacle with the one on the leeward side being the largest. The flow is directed towards negative z only on the windward side. Due to the staggered configuration, the flow encounters the obstacles as a narrow region where it is accelerated and horizontal components are added to the recirculation regions on those sides of the obstacle.

The variances of the velocity components, shown in panels d)–f), indicate that most of the turbulence within the roughness sublayer is generated from the vortex shedding at the top of the obstacle. This is then transported downwards by the recirculation regions identified from the mean velocities. Further turbulence production can be identified on the vertical sides of the obstacle where the vertical velocity is towards positive z and in the region between two obstacles where flow is accelerated by the constricted geometry and sheared by the horizontal recirculation regions. There is also a patch of high variance of the v component of velocity near the bottom surface at around $x = 60$ m. This turbulence is, at least partially, transported from the vortex shedding layer above by the vertical motions in the recirculation region in the leeward side of the obstacle.

Figures 7 and 8 provide a view on the errors due to using time averaging instead of ensemble averaging by showing the root-mean-square (RMS) differences between the ensemble average and the long time average (210 min). The errors are the largest above the obstacles where the large scale mean wind and the wind turning have their strongest effect. Both horizontal wind components are affected as well as the variance in the y direction. Within the obstacles, the biggest errors are in the vicinity of the windward face of the obstacle. Regions of elevated error can be seen where the flow is deflected along the y axis and at the narrowest part of the geometry between two obstacles. By comparing the RMS differences in Fig. 7 and 8 with Fig. 5 and 6, high variance can be seen at the same areas. The errors in regions directly at the windward face and on the

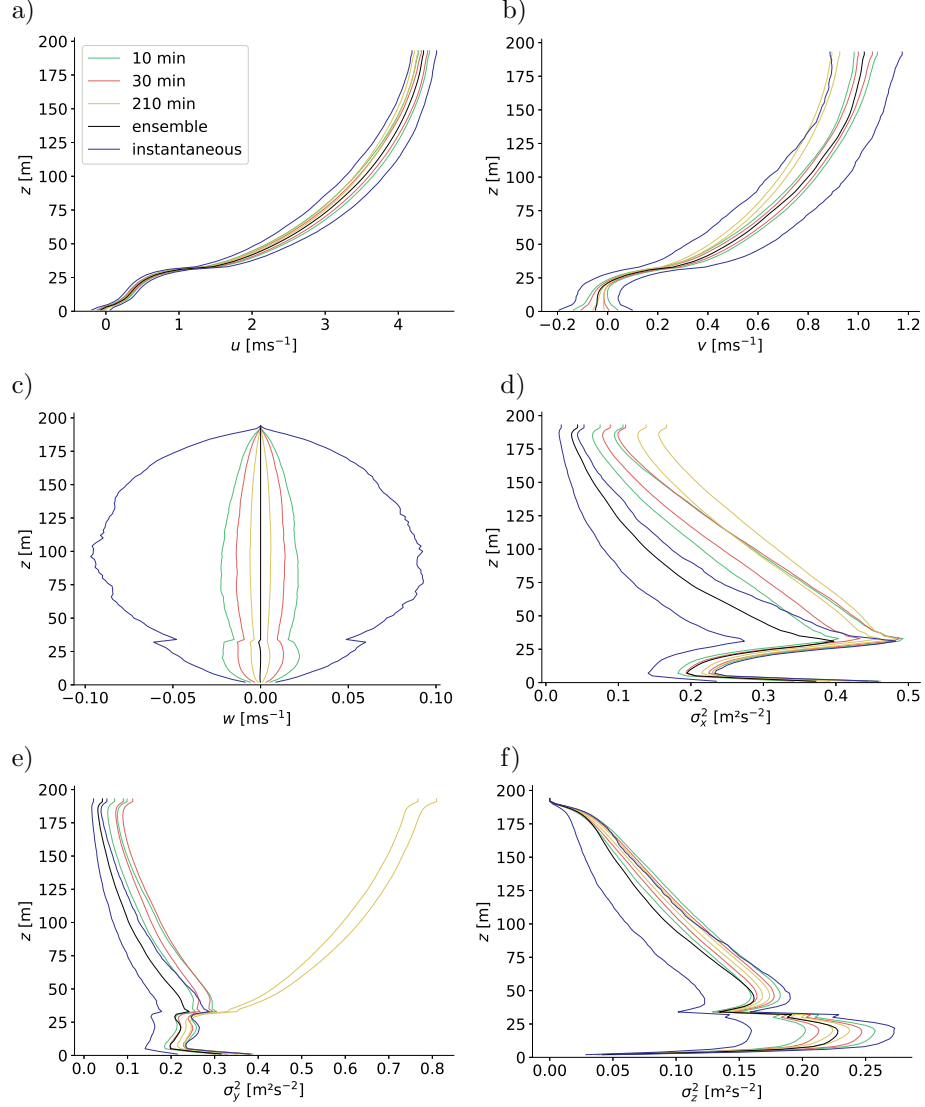


Figure 4: Vertical wind profiles in the case of the staggered cube array. a) Velocity along x axis (u), b) velocity along y axis (v), c) velocity along z axis (w), d) variance of u (σ_x^2), e) variance of v (σ_y^2), and variance of w (σ_z^2). All quantities have been averaged over the horizontal directions. The black line indicates the ensemble mean while the other lines indicate the 25th and 75th percentile for different time averaging intervals. All time averages are centred around the mid point of the simulation, at $t = 120$ min

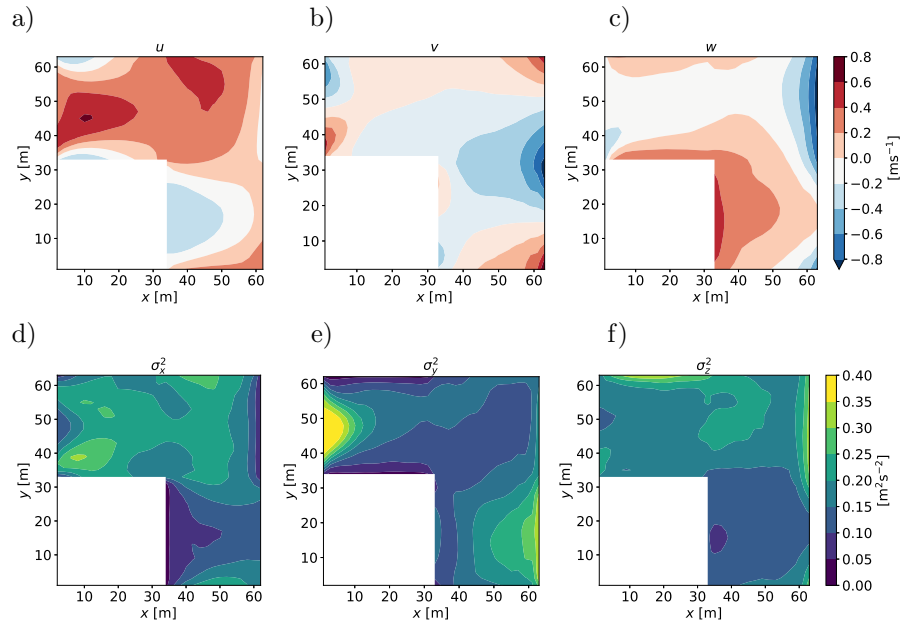


Figure 5: Ensemble-averaged velocity and variances for a horizontal plane through the roughness elements in the staggered cube array at $z = 16$ m and $t = 120$ min. a) Velocity along x axis (u), b) velocity along y axis (v), c) velocity along z axis (w), d) variance of u axis (σ_x^2), e) variance of v (σ_y^2), and variance of w axis (σ_z^2).

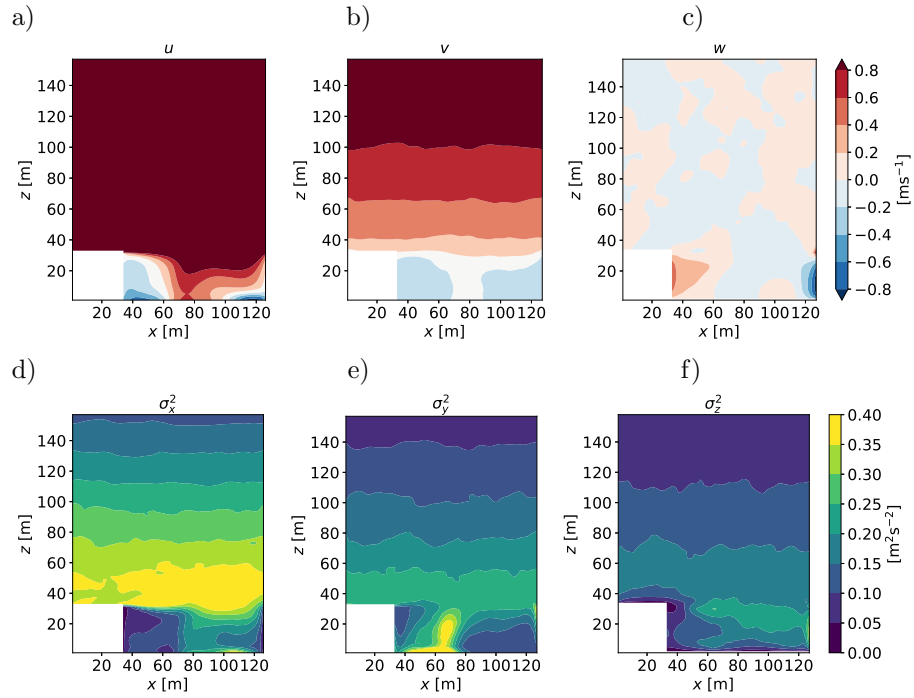


Figure 6: Ensemble-averaged velocity and variances for a vertical plane through the roughness elements for the staggered cube array at $y = 16$ m for $0 \text{ m} \leq x \leq 64$ m and at $y = 48$ m for $64 \text{ m} \leq x \leq 128$ m and $t = 120$ min. a) Velocity along x axis (u), b) velocity along y axis (v), c) velocity along z axis (w), d) variance of u (σ_x^2), e) variance of v (σ_y^2), and variance of w (σ_z^2)

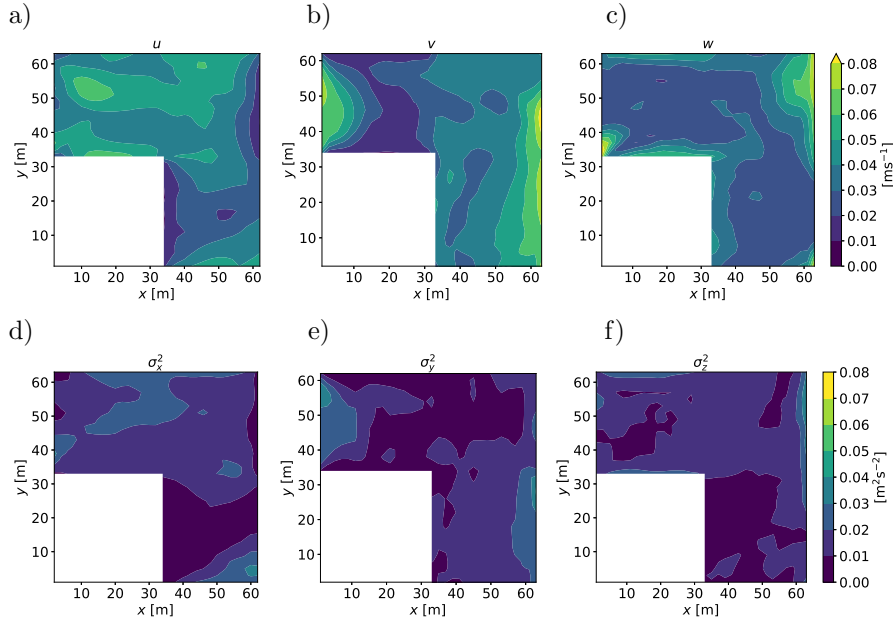


Figure 7: RMS Difference between the ensemble velocity and the long (210 min) time average for a horizontal plane through the roughness elements in the staggered cube array at $z = 16$ m. a) Velocity along x axis (u), b) velocity along y axis (v), c) velocity along z axis (w), d) variance of u (σ_x^2), e) variance of v (σ_y^2), and variance of w (σ_z^2)

bottom boundary in front of it can thus be attributed, at least partly, to turbulence from the shear layer that has been transported down by the recirculation region.

To quantify the errors due to use of time-averaging instead of an ensemble average, we utilize Taylor diagrams (Taylor 2001; Chang and Hanna 2004). These polar plots have normalized standard deviation (NSD) on the radial axis and the correlation coefficient (R) as the azimuthal coordinate. A perfect model has $R = NSD = 1$ and the distance from this point is the normalized root-mean-square error (NRMSE). We calculate the Taylor diagrams using only the roughness sublayer i.e. the flow below the height of $4h = 128$ m. Above the roughness sublayer the flow field is not sensitive to the details of individual roughness elements and spatial averaging in the horizontal directions can be utilized instead of ensemble or time averaging. One has to keep in mind, however, that the use of spatial averaging requires that there are no deviations from homogeneity in the roughness pattern on the scales much larger than the representative size of the roughness elements.

The effect of averaging time on the error as compared to the ensemble mean

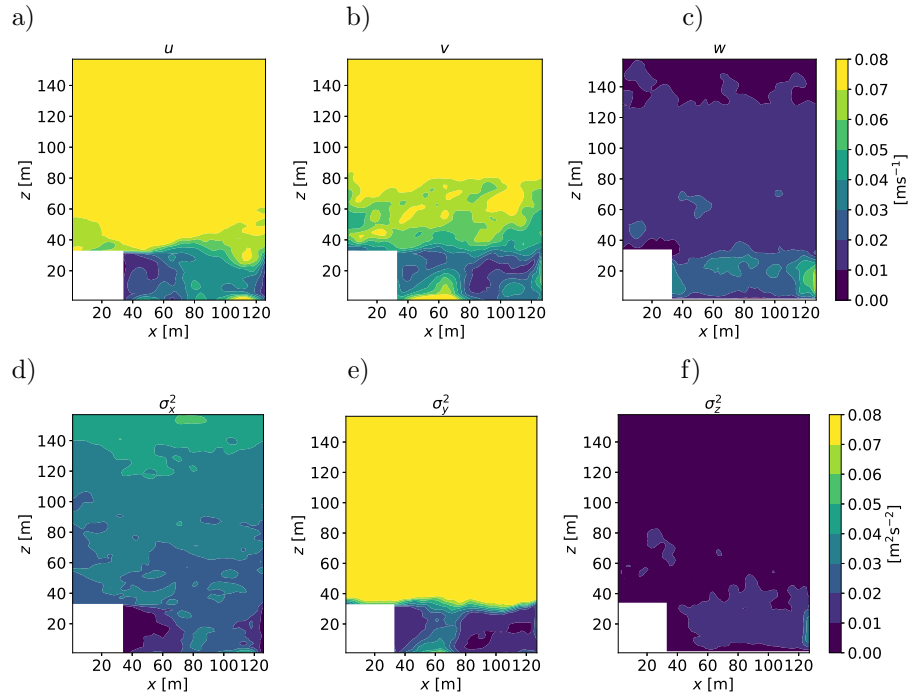


Figure 8: RMS Difference between the ensemble velocity and the long (210 min) time average for a vertical plane through the roughness elements at $y = 16$ m for $0 \text{ m} \leq x \leq 64 \text{ m}$ and at $y = 48 \text{ m}$ for $64 \text{ m} \leq x \leq 128 \text{ m}$ and $t = 120 \text{ min}$. a) Velocity along x axis (u), b) velocity along y axis (v), c) velocity along z axis (w), d) variance of u (σ_x^2), e) variance of v (σ_y^2), and variance of w (σ_z^2)

is shown in Fig. 9 a)–c) for the mean velocity components. Each dot represents an ensemble member and the colours indicate different averaging periods. For all components, a longer averaging time results in a smaller variation within the ensemble. However, in the case of v component, the 150 and 210 minute averages show a larger error than the 90 minute average due to decrease in NSD. Nevertheless, time-averaging appears to improve the accuracy of the mean velocity components for averaging times up to 90 minutes and even after that the error is not very large. Averaging over the whole duration of the simulation with a changing wind direction hence does not have a major effect on the mean velocity components.

The variances, shown similarly in Fig. 9 d)–f), display a mixed behaviour with respect to performance increase with time averaging. Firstly, the variation between the simulations is much larger than with the averages. Secondly, both the u and the v component of variance show deteriorated accuracy for longer time statistics beyond 150 minutes and 50 minutes, respectively. Furthermore, the accuracy of the v variance decreases catastrophically for averaging periods longer than 90 minutes. The errors for 150 minute and 210 minute v variances are so large that they are outside the plot shown in panel e). The variance of w , however, appears well-behaved and averaging over any length of time improves the statistic.

The error measures included in the Taylor diagram (NSD, R, and NRMSE) are indicators of unsystematic errors only (Chang and Hanna 2004) and hence a Taylor diagram might give a false impression of the performance of the simulations. Fractional bias (FB) is a statistical performance measure that accounts systemic bias only (Chang and Hanna 2004). It can be used to complement the Taylor diagram for a better overall view of the biases. For a perfect match with reference results, $FB=0$.

To explore the systematic errors, we have calculated the FB for the same time-averaging intervals as in the Taylor diagram in Fig. 9 and the interquartile ranges are shown in the upper half of Table 1. Both u and v display a similar performance measured with FB as they did in the Taylor diagram. The FB decreases for both components with increasing averaging time until 90 minutes. After that, the performance of v decreases faster than the performance of u . The interquartile range of the vertical component w , however, does not tell much about the biases but more about the failure of FB for this case. The FB is calculated using a fraction and because the mean of w is zero for large parts of the domain, division by very small numbers is heavily influencing this case.

Based on the interquartile ranges of FB, the systematic errors in variances behave in a similar manner to the unsystematic errors as indicated by the Taylor diagram in Fig. 9. The systematic biases in the variance of u decrease until 150 minutes and are relatively small even for the 210 minute averaging-time while in the case of w variance the smallest interquartile range of FB is reached at 210 minutes. The variance of v shows improvement in FB until 30 minute averaging-time and deterioration after that. As with the Taylor diagrams, 150 minute and 210 minute time averages show a very poor performance.

The statistical convergence of an ensemble can be improved by utilizing time-

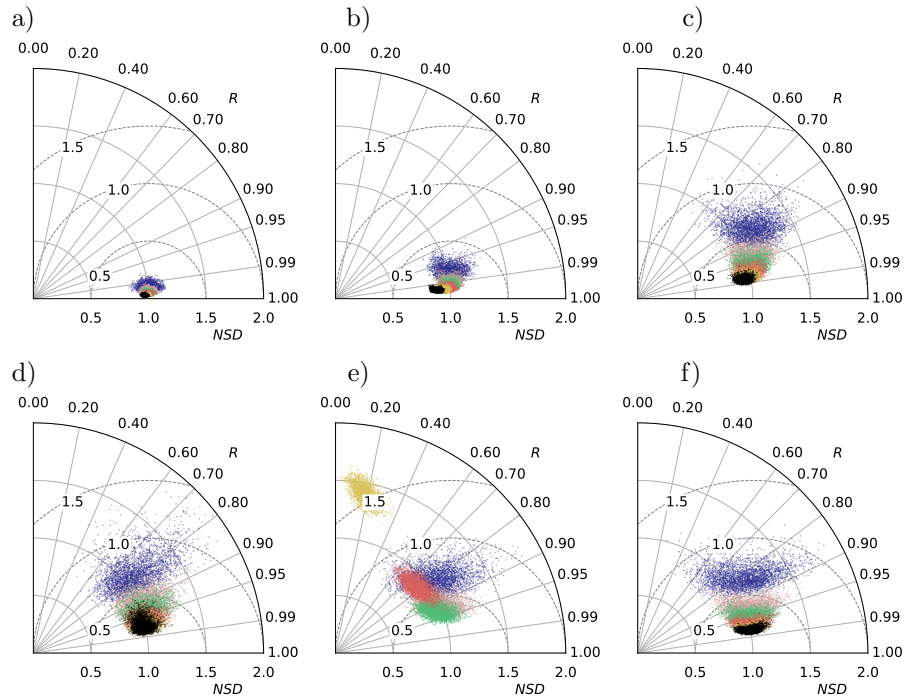


Figure 9: Taylor diagrams for the mean (a–c) and variance (d–f) of u , v , and w components of velocity with different averaging intervals in the case of the staggered cube array. The ensemble mean calculated with instantaneous values is used as the reference. The polar plot has normalized standard deviation as the radial axis and correlation as the azimuthal coordinate. The circles drawn using a dashed lines indicate normalized root mean square error with a perfect model at point (1,1). Each dot indicates an ensemble member and the colours indicate different averaging intervals for 10 min (blue), 30 min (pink), 50 min (green), 90 min (red), 150 min (yellow), and 210 min (black). Note that in e) the 150 min and 210 min values are (mostly) outside the plot area and not shown for this reason

Table 1: The interquartile ranges of Fractional bias of ensembles with different time-averaging and of ensembles with different sizes in the case of the cube array.

		u	v	w
mean	10 min	[-0.036, 0.040]	[-0.045, 0.048]	[-2.012, -1.988]
	30 min	[-0.019, 0.025]	[-0.027, 0.028]	[-2.019, -1.982]
	50 min	[-0.014, 0.021]	[-0.014, 0.027]	[-2.023, -1.972]
	90 min	[-0.005, 0.021]	[-0.007, 0.038]	[-2.032, -1.966]
	150 min	[0.007, 0.027]	[0.051, 0.079]	[-2.042, -1.956]
	210 min	[0.017, 0.039]	[0.111, 0.152]	[-2.045, -1.955]
variance	10 min	[0.048, 0.230]	[-0.022, 0.093]	[-0.015, 0.086]
	30 min	[0.006, 0.119]	[-0.055, 0.016]	[-0.013, 0.046]
	50 min	[-0.013, 0.074]	[-0.104, -0.047]	[-0.011, 0.036]
	90 min	[-0.024, 0.042]	[-0.261, -0.218]	[-0.011, 0.023]
	150 min	[-0.045, 0.013]	[-0.560, -0.523]	[-0.010, 0.016]
	210 min	[-0.070, -0.009]	[-0.841, -0.795]	[-0.012, 0.011]
mean	2 members	[-0.013, 0.018]	[-0.019, 0.020]	[-2.027, -1.973]
	5 members	[-0.008, 0.012]	[-0.012, 0.011]	[-2.045, -1.956]
	10 members	[-0.006, 0.009]	[-0.009, 0.010]	[-2.058, -1.934]
	25 members	[-0.003, 0.006]	[-0.005, 0.005]	[-2.094, -1.903]
	50 members	[-0.001, 0.005]	[-0.004, 0.004]	[-2.137, -1.859]
	100 members	[-0.000, 0.004]	[-0.003, 0.003]	[-2.178, -1.795]
variance	2 members	[-0.003, 0.082]	[-0.052, -0.003]	[-0.011, 0.030]
	5 members	[-0.011, 0.044]	[-0.048, -0.017]	[-0.008, 0.020]
	10 members	[-0.006, 0.032]	[-0.043, -0.023]	[-0.005, 0.015]
	25 members	[-0.002, 0.022]	[-0.041, -0.027]	[-0.000, 0.011]
	50 members	[0.001, 0.017]	[-0.040, -0.029]	[0.000, 0.009]
	100 members	[0.002, 0.014]	[-0.038, -0.031]	[0.002, 0.007]

averaged values instead of instantaneous values. In an earlier study concerning a forest edge flow, Kanani et al. (2014) showed that a ten-member ensemble is sufficient for their case with 15 minute time-averaging window. The compromise between the deterioration of accuracy due to time-averaging and the cost of producing a large ensemble can be expected be different in different flow cases. Based on our results, time-averaged statistics using an averaging-interval of 30 minutes appears most suitable as these show decreased variation together with only minor deviations from the reference result.

We examine the errors in different ensemble sizes of 30-minute statistics using Taylor diagrams, shown in Fig. 10, and tabulated interquartile ranges of FB, shown in the lower half of Table 1. We consider ensembles ranging from two to 100 members and for each averaging time, 1 000 different ensembles are sampled. Each dot in Fig. 10 represents an ensemble that has been sampled from the available ensemble members of the full ensemble.

For all components of both the mean and variance, a steady convergence towards a smaller error can be seen in the Taylor diagram in Fig. 10. As expected, the mean variables show less variation at all averaging times compared to the variances. The w component of mean velocity shows the largest variation at small ensemble sizes and hence benefits the most from increasing ensemble size. A similar behaviour can be observed for all components of variance. Disregarding the mean of w , the interquartile ranges of FB in Table 1 agree with this observation. There are very few changes in the metrics between 50 and 100 members and not very much between 25 and 50 members. An ensemble size of 10–50 members could thus be a good compromise between computational burden and accuracy when used together with 30 minute time averaging.

3.2 Realistic Urban Environment

In the case of the realistic urban environment, we have carried out a 24 hour 20 minutes long spinup simulation with constant pressure gradient directed at 240° . The simulation was started using only the largest domain in order to speed up to spinup process. The two-way coupled, three-domain setup was included after eight hours single-domain spinup. The kinetic energy content within the largest domain, shown in Fig. 11 a) using the black line, develops quickly for the first five hours and then levels off. We interpret this as the flow reaching a fully developed state at the largest domain and switch on the two-way coupled intermediate and small domains after eight simulated hours. This results in a small jump in the kinetic energy content on the largest domain and in a large jump in the smallest domain, as shown in Fig. 11 b). The kinetic energy content stabilizes at approximately 10 hours although there are clear small-scale, turbulent variations visible in the smallest domain.

Two-way coupled, three-domain simulations with a turning pressure gradient are branched off every 20 minutes from the spinup starting at 16 hours of simulated time. In total, an ensemble of 50 simulations with a turning pressure gradient are carried out. As there are no repeating units in the realistic urban environment, the total ensemble size is the same as the number of simulations.

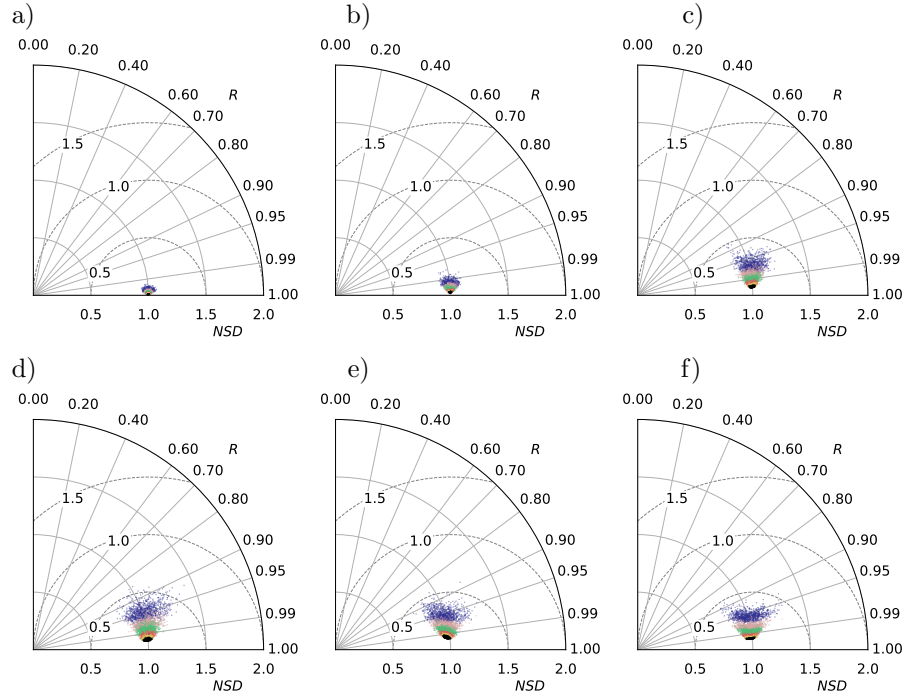


Figure 10: Taylor diagrams for ensembles with different sizes calculated using 30 minute mean (a–c) and variance (d–f) of u , v , and w components of velocity for the case of staggered cube-array. The ensemble mean calculated with instantaneous values is used as the reference. The polar plot has normalized standard deviation as the radial axis and correlation as the azimuthal coordinate. The circles drawn using a dashed lines indicate normalized root mean square error with a perfect model at point (1,1). Each dot indicates an ensemble and the colours indicate different ensemble sizes: 2 members (blue), 5 members (pink), 10 members (green), 25 members (red), 50 members (yellow), and 100 members (black)

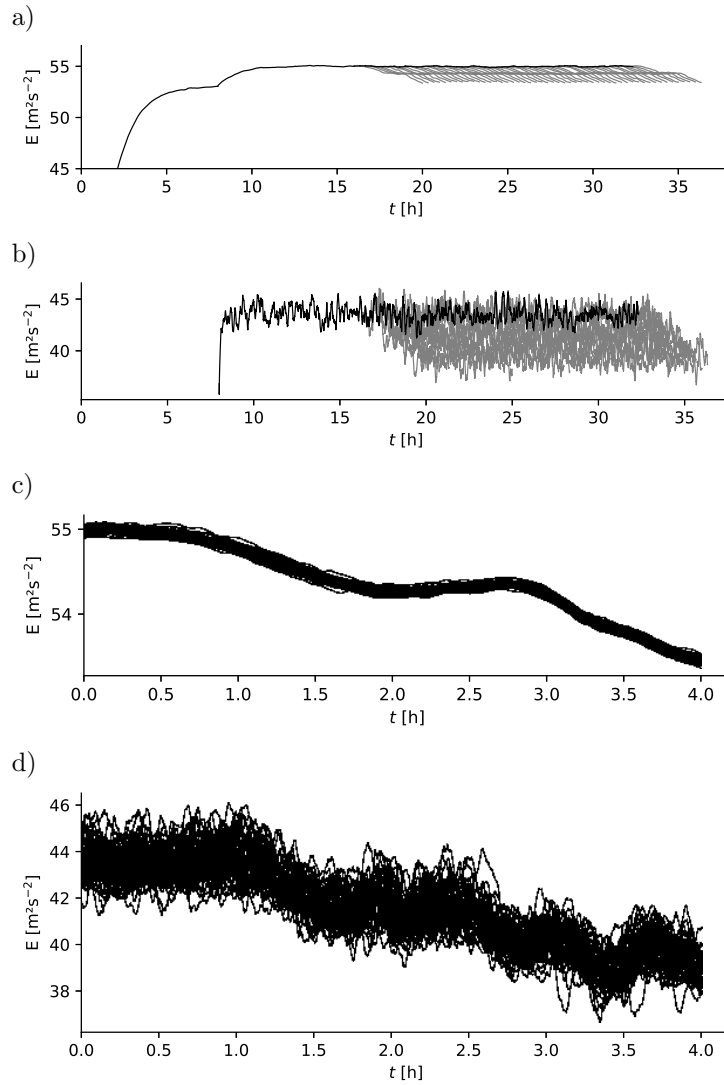


Figure 11: Resolved kinetic energy content of the realistic urban environment simulations. The turning pressure gradient simulations branch off from the spinup every 20 minutes starting at 18 hours since the beginning of the spinup. a) The spinup simulation (black) and the simulations with a turning pressure gradient (grey) for the largest simulation domain. b) The spinup simulation (black) and the simulations with a turning pressure gradient (grey) for the innermost simulation domain. c) All turning pressure gradient simulations for the largest domain shown using time since start of pressure gradient turning. d) All turning pressure gradient simulations for the innermost domain shown using time since start of pressure gradient turning

The spinup simulation consumed approximately 61 000 processing element hours in total while each of the turning pressure gradient simulations required approximately 9 800 core hours on average.

The direction of the pressure gradient was at 240° at the beginning of the simulation and 300° at the end of the simulations. The mean wind direction, calculated using the upper parts of the largest domain (not shown), was initially 239° and followed the pressure gradient with a lag in a similar manner to the cube array case. However, the acceleration of the wind direction was slower. The faster acceleration at the beginning of the simulation lasted until 60 minutes when the approximate turning speed of 8°h^{-1} was reached. For the rest of the simulation, there was a slower acceleration for the turning speed of the wind so that at the end of the simulation the turning speed was approximately 12°h^{-1} . At the middle of the simulation the wind direction was 251° and 271° at the end of the simulation.

The kinetic energy content for the simulations with a turning pressure gradient are shown branching off from the spinup in Fig. 11 a) and b) using gray lines. Panels c) and d) show the kinetic energy content of these simulations for time since the start of turning. For all simulations, the kinetic energy content shows an overall decrease during the simulations. We interpret this to reflect the overall topography of the simulated domain: the river valley at the centre of the domain as well as the bays within the archipelago are all aligned in approximately northeast–southwest direction as a result of the latest ice age, as can be seen from the topography in Fig. 2. The flow is expected to encounter less form drag due to channeling effects when it is approximately aligned with these large scale structures of the simulated terrain.

The variation between the ensemble members appears stronger in the innermost domain than in the largest domain. We expect the stronger variation to be due to a larger share of resolved turbulence, created by the roughness elements, in the innermost domain. To quantify this variation, we normalized the kinetic energy content using time and ensemble-averaged kinetic energy and calculated the ensemble variance for each time instant. With this, we observed (not shown) that the ensemble has three orders of magnitude less variation in the largest domain than in the innermost domain. A comparable measure can be extracted from the staggered cube array ensemble by sampling the simulations and the repeating units. Using 64 randomly selected repeating units from all simulations and a thousand 50 member ensembles, we observe the normalized mean variance to be of the same order as in the case of the innermost domain in the realistic flow. For the remainder of the article, we focus on the innermost domain only.

Nevertheless, a decrease in variation between the ensemble members, compared to the staggered cube array, can be seen in the vertical mean wind and variance profiles for the innermost domain at 120 minutes since the start of pressure gradient turning, shown in Fig. 12. This is clearest in the mean velocity along the x direction where an almost full overlap of the ensemble mean (shown using a black line) and the limits of the interquartile range (shown using blue lines). Other velocity components and the variances also display a narrower

interquartile range than in the case of the cube array. The spread between the ensemble members is largest at the upper end of the domain. Nevertheless, the overall shape of the profiles is typical for an urban flow: the vertical extent of the roughness elements is indicated by a jump in the lower part of the mean velocity profiles and can also be seen in the variances profiles.

The effects of time-averaging are similar to the cube array setup for the vertical profiles. In the velocity components, the ensemble average is mostly within the interquartile range of the 10 minute time-averaged simulations. With 30 minute time-averages, the ensemble mean is partially outside the interquartile range when the variances are considered. The long, 210 minute time-average fails to capture the ensemble average in almost all cases and especially at the upper parts of the domain. The largest deviation from the ensemble mean is observed in the v component and especially in the variance where catastrophic deterioration of the solution is seen for the long averaging time.

The ensemble of 50 members does not appear to be large enough for mean velocity and variance when instantaneous values are considered. Figure 13 displays the ensemble mean velocity and velocity variances for the x component at $z = 40$ m in the smallest simulated domain. The insufficient ensemble size is visible as the sharp variations in the mean velocity field and as static noise type patterns in the variance field. Other velocity and variance components behave in a similar manner (not shown).

An improved ensemble average can be achieved using 30 min averages instead of the instantaneous values, as suggested by the results of the cube array. This is seen from the ensemble mean velocity and velocity variances at $z = 40$ m in the smallest simulated domain, shown in Fig. 14. The velocity and the variance fields are not fully smooth but clearly smoother than when instantaneous values are used. The static noise pattern has disappeared from the variance fields.

The overall flow field through the roughness elements is very typical for the considered urban flow. The plane shown in Fig. 14 cuts through some of the buildings and the orography, especially in the southeastern quadrant of the domain, and their effects on the flow are clearly visible. There is strong, large-scale channelling along the less obstructed parts on the northwestern quarter of the domain, seen as strong u and v velocity components. Channelling is visible also in the southeastern quadrant of the domain in street canyons and other minor openings that are aligned with the main flow direction. The roughness elements affect the flow also by reducing the mean wind speed and increasing variances in their wakes through the turbulence they generate, especially in the southeastern quadrant of the domain where the terrain is more elevated and where there are more buildings. The variances are strong in the wake especially when there are no further obstacles downstream.

The direct utilisation of long time-averaging can cause significant errors localized around the wakes of the roughness elements. This is seen from Fig. 15 where the RMS difference between the ensemble averages, calculated using 30 minute average values, and the long 210 minute time average is shown. Depending on the quantity, different regions display the largest errors. In the case of mean horizontal velocity components, the regions of the highest error form

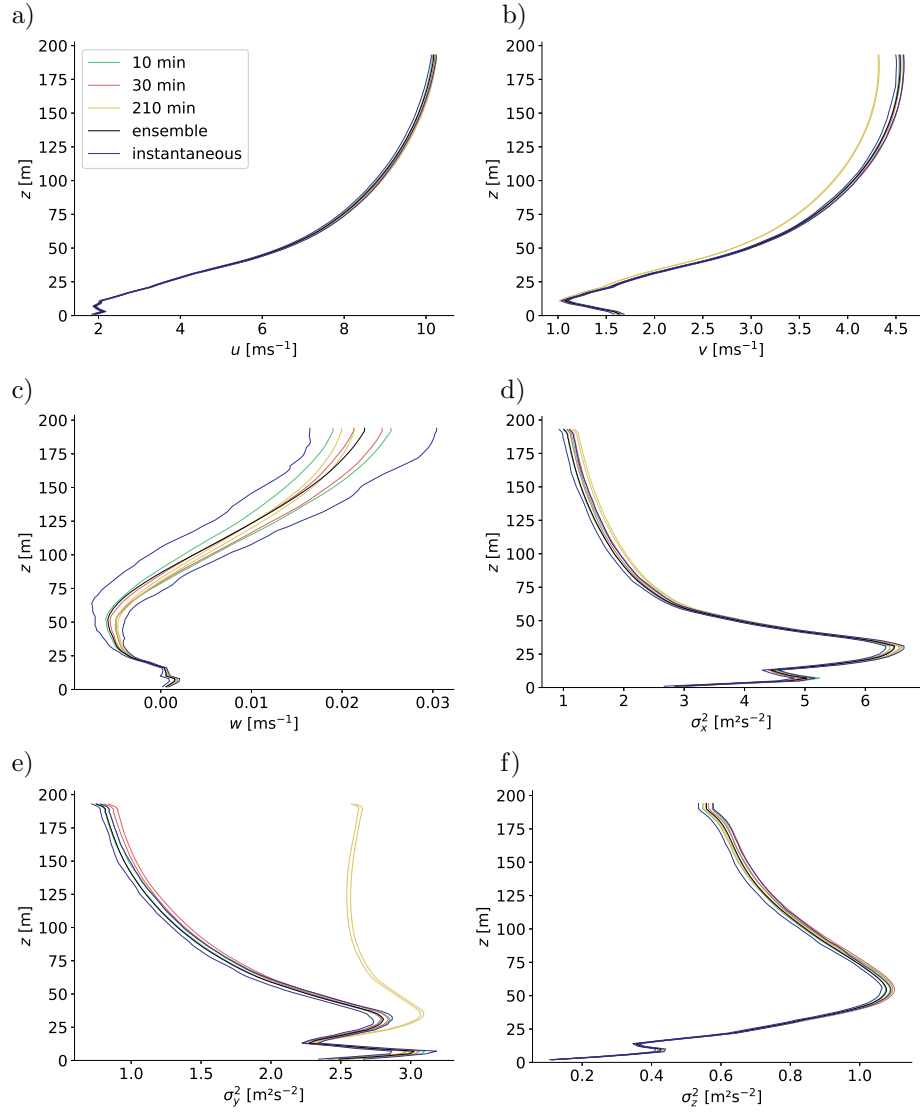


Figure 12: Vertical wind profiles in the innermost domain in the case of the realistic urban flow: a) Velocity along x axis (u), b) velocity along y axis (v), c) velocity along z axis (w), d) variance of u axis (σ_u^2), e) variance of v axis (σ_v^2), and variance of w axis (σ_w^2). All quantities have been averaged over the horizontal directions. The black line indicates the ensemble mean while the other lines indicate the 25th and 75th percentile for different time averages with blue denoting no time averaging, green a short time average (10 min), the red a medium time average (30 min), and the yellow a long time average (210 min). Time averaging is centred around 120 minutes from the start of the turning of the pressure gradient

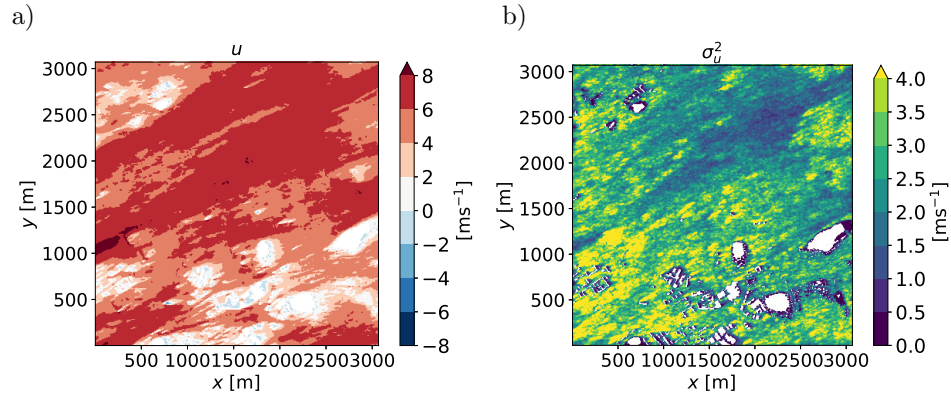


Figure 13: Ensemble-averaged velocity component u calculated using instantaneous values for a horizontal plane through the roughness elements at $z = 40$ m for the innermost domain in the case of the realistic urban flow. a) mean and b) variance

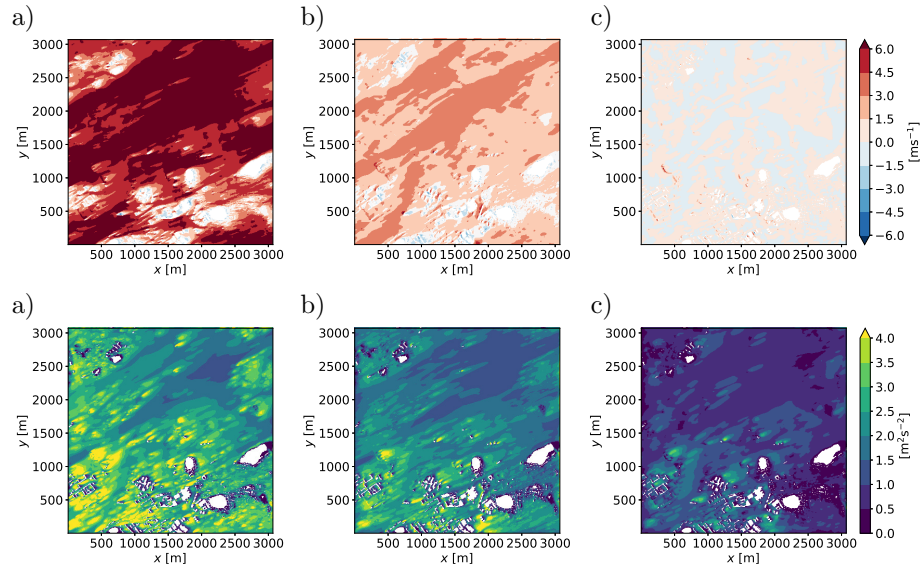


Figure 14: Ensemble-averaged velocity calculated using 30 minute time-averages for a horizontal plane through the roughness elements at $z = 40$ m for the innermost domain in the case of the realistic urban flow. a) mean of u , b) mean of v , c) mean of w , d) variance of u , e) variance of v , and f) variance of w

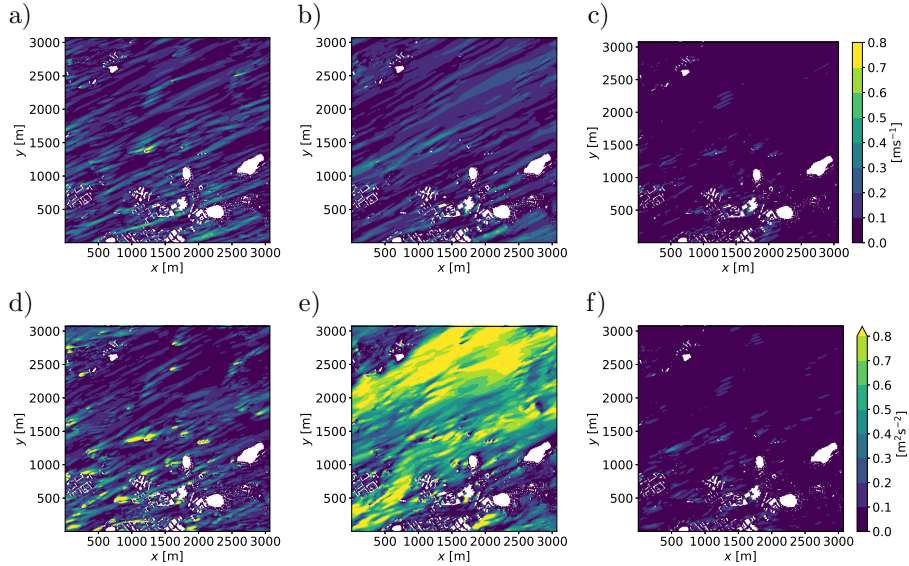


Figure 15: RMS Difference between the ensemble velocity and the long (210 min) time average for a horizontal plane through the roughness elements at $z = 40$ m for the innermost domain in the case of the realistic urban flow. a) mean of u , b) mean of v , c) mean of w , d) variance of u , e) variance of v , and f) variance of w

long structures in the wakes of the roughness elements. We interpret this as the inability of the long averaging interval to accurately capture the changing direction of the wake. The vertical mean velocity w , its variance and the u variance have their largest errors in the immediate vicinity of the roughness elements. This is probably due to smoothed out small time-scale variation of the recirculation regions and other smaller flow features caused by the roughness elements. Finally, the v variance has its largest errors in the areas where the mean v velocity is at its largest, at the open areas mostly located in the northern half of the domain.

As in the case of the cube array, we utilize Taylor diagrams to evaluate the effect of averaging time on the simulation performance. We consider again only the roughness sublayer, here defined using the average height of the roughness elements in the domain: $4h_{\text{avg}} = 84$ m. The low variation between the ensemble members that was observed earlier is clearly visible also in the Taylor diagrams in Fig. 16 where each dot represents an ensemble member and the colours denote different averaging intervals. Especially with mean velocity components, all ensemble members are located in tight bundles for all averaging intervals, indicating similar R and NSD values.

Similar error behaviour as with the cube array can be observed here with

Table 2: The interquartile ranges of fractional bias of ensembles with different time-averaging intervals for the innermost domain in the case of the realistic urban flow

		u	v	w
mean	10 min	[-0.002, 0.010]	[-0.008, 0.006]	[-0.223, 0.142]
	30 min	[-0.004, 0.003]	[-0.004, 0.005]	[-0.091, 0.115]
	50 min	[-0.001, 0.003]	[0.006, 0.010]	[0.064, 0.167]
	90 min	[-0.001, 0.003]	[0.006, 0.010]	[0.064, 0.167]
	150 min	[-0.002, 0.000]	[0.023, 0.027]	[0.036, 0.105]
	210 min	[-0.004, -0.001]	[0.052, 0.055]	[0.059, 0.144]
variance	10 min	[0.054, 0.085]	[0.038, 0.056]	[0.010, 0.028]
	30 min	[0.009, 0.027]	[-0.001, 0.015]	[-0.001, 0.010]
	50 min	[-0.007, 0.002]	[-0.059, -0.051]	[0.001, 0.010]
	90 min	[-0.007, 0.002]	[-0.059, -0.051]	[0.001, 0.010]
	150 min	[-0.028, -0.020]	[-0.184, -0.177]	[-0.001, 0.006]
	210 min	[-0.048, -0.041]	[-0.324, -0.315]	[-0.002, 0.003]

the realistic urban case with increasing averaging time: the error decreases with increasing averaging time until 30 or 50 minutes depending on the quantity and increases for longer averaging times. This effect is minor for all other quantities except for variance of v where the 150 and 210 minute values displays a clearly poorer performance on the correlation. However, one has to keep in mind that the Taylor diagram was created using a small ensemble that was calculated with 30 minute averages as the reference value. This can be expected to result in improved performance for, at least, the 30 minute and 50 minute averaging times.

The interquartile ranges of FB, shown in Table 2, mostly agree with observations from the Taylor diagram in Fig. 10. The best performance is from the 30 minute time-averages and the worst performance can be seen in the 150 and 210 minute variances of v . Unlike in the staggered cube array, FB does not fail in describing the systematic bias in mean w . Nevertheless, FB displays similar development on the reliability of mean w as the measures in the Taylor diagram.

4 Conclusions

We have studied the differences between time-averaged and ensemble-averaged statistics on a flow with a temporally turning pressure gradient in the simplified case of a staggered cube array and in the case of a realistic urban flow past the city of Turku, Finland. The staggered cube array consisted of a 648 repeating elements, which we used together with five individual simulations to create an ensemble of 3 240 member. In the case of the realistic urban flow, there were no repeating elements and hence the ensemble size was the same as the number of

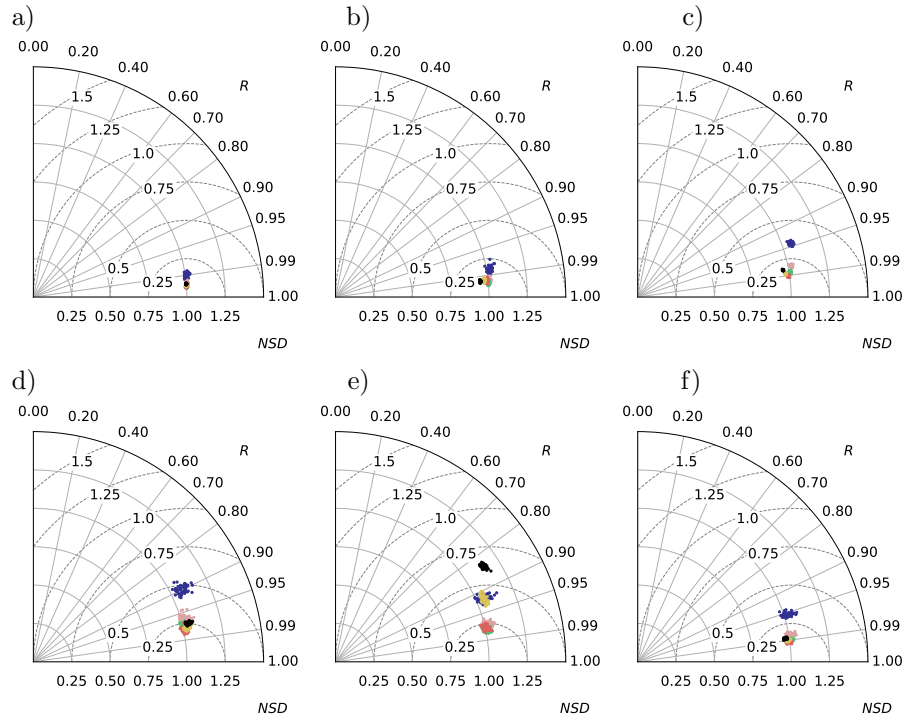


Figure 16: Taylor diagrams for the mean (a–c) and variance (d–f) of u , v , and w components of velocity with different averaging intervals for the innermost domain in the case of the realistic urban flow. The ensemble mean calculated with 30-minute time-averages is used as the reference. The polar plot has normalized standard deviation as the radial axis and correlation as the azimuthal coordinate. The circles drawn using a dashed lines indicate normalized root mean square error with a perfect model at point (1,1). Each dot indicates an ensemble member and the colours indicate different averaging intervals for 10 min (blue), 30 min (pink), 50 min (green), 90 min (red), 150 min (yellow), and 210 min (black)

simulations: 50.

Our results indicate that, in the case of a turning pressure gradient, significant errors can contaminate the results if one disregards the transient aspects of the flow and accumulates mean wind and variances throughout the simulation. The mean velocity of the main (strongest) wind components remains mostly unaffected but all other wind components and variances are affected. The largest departures from the ensemble velocity were observed in the weaker wind component (here v) and especially in its variance.

Our results on the cube array indicate that the deterioration of the time-averaged statistics can be mitigated by combining time-averaging and ensemble averaging. In our case with a turning speed of 15°h^{-1} for the pressure gradient, corresponding to wind direction turning speed of 12°h^{-1} for the cube array and 8.8°h^{-1} for the realistic urban environment, time averaging up to 30 minutes shows an increase in solution accuracy. The corresponding change in the mean wind direction was 5.8° in the cube array case and 4.4° in the case of the realistic urban environment. Furthermore, an ensemble of 10–50 members combined with time-averaging up to 30 minutes appeared to provide the best compromise between accuracy and ensemble size. This guideline is most useful in the roughness sublayer. Above it, spatial averaging in the horizontal direction can be utilized together with instantaneous fields to obtain sufficiently well-converged statistics, provided that the flow is otherwise homogeneous.

Using a 50 member ensemble together with a 30-minute statistics, we analysed the spatial error distribution in the vicinity of the roughness elements in the case of the realistic urban flow. When long time-averaging procedures are used, the wake regions of the roughness elements show the biggest errors. This is due to both the change of wind direction, and hence the wake direction, but also due to the small, unsteady features within the wakes. Variance of the weaker wind component (here v) was predicted incorrectly by long time-averaging in high-wind areas.

5 Data Availability

The data produced and used in this publication are openly available through the research data repository of the Finnish Meteorological Institute (Keskinen and Hellsten 2025).

Acknowledgements

The research is a part of the RESPONSE project. This project has received funding from the European Union’s Horizon 2020 research and innovation programme under grant agreement No 957751. The research has also received funding from the European Union’s Horizon 2020 research and innovation programme under the Marie Skłodowska-Curie grant agreement No 872931 through the YADES project. The authors wish to acknowledge CSC – IT Center for Sci-

ence, Finland, for generous computational resources. The authors also acknowledge the City of Turku and the National Land Survey of Finland for providing us with surface elevation data.

References

- Ahn J, Lee JH, Sung HJ (2013) Statistics of the turbulent boundary layers over 3D cube-roughened walls. *International Journal of Heat and Fluid Flow* 44:394–402, DOI 10.1016/j.ijheatfluidflow.2013.07.010
- Ahola J, Raatikainen T, Alper ME, Keskinen JP, Kokkola H, Kukkurainen A, Lipponen A, Liu J, Nordling K, Partanen AI, Romakkaniemi S, Räisänen P, Tonttila J, Korhonen H (2022) Technical note: Parameterising cloud base updraft velocity of marine stratocumuli. *Atmospheric Chemistry and Physics* 22(7):4523–4537, DOI 10.5194/acp-22-4523-2022
- Blackman K, Perret L, Savory E (2015) Effect of upstream flow regime on street canyon flow mean turbulence statistics. *Environmental Fluid Mechanics* 15(4):823–849, DOI 10.1007/s10652-014-9386-8
- Chang JC, Hanna SR (2004) Air quality model performance evaluation. *Meteorology and Atmospheric Physics* 87(1):167–196, DOI 10.1007/s00703-003-0070-7
- Cheng WC, Porté-Agel F (2015) Adjustment of Turbulent Boundary-Layer Flow to Idealized Urban Surfaces: A Large-Eddy Simulation Study. *Boundary-Layer Meteorology* 155(2):249–270, DOI 10.1007/s10546-015-0004-1
- Chow FK, Street RL (2009) Evaluation of Turbulence Closure Models for Large-Eddy Simulation over Complex Terrain: Flow over Askervein Hill. *Journal of Applied Meteorology and Climatology* 48(5):1050–1065, DOI 10.1175/2008JAMC1862.1
- Dauxois T, Peacock T, Bauer P, Caulfield CP, Cenedese C, Górlé C, Haller G, Ivey GN, Linden PF, Meiburg E, Pinardi N, Vriend NM, Woods AW (2021) Confronting Grand Challenges in environmental fluid mechanics. *Physical Review Fluids* 6(2):020,501, DOI 10.1103/PhysRevFluids.6.020501
- Deardorff JW (1980) Stratocumulus-capped mixed layers derived from a three-dimensional model. *Boundary-Layer Meteorology* 18(4):495–527, DOI 10.1007/BF00119502
- Eyring V, Bony S, Meehl GA, Senior C, Stevens B, Stouffer RJ, Taylor KE (2016) Overview of the Coupled Model Intercomparison Project Phase 6 (CMIP6) experimental design and organisation. *Geoscientific Model Development* 9:1937–1958, DOI 10.5194/gmdd-8-10539-2015

- Giometto MG, Christen A, Egli PE, Schmid MF, Tooke RT, Coops NC, Parlange MB (2017) Effects of trees on mean wind, turbulence and momentum exchange within and above a real urban environment. *Advances in Water Resources* 106:154–168, DOI 10.1016/j.advwatres.2017.06.018
- Gropp W, Lusk E, Skjellum A (1999) Using MPI: Portable parallel programming with the message passing interface, 2nd edn. MIT Press
- Hackbusch W (1985) Multigrid methods and applications, Springer, p 378
- Hagishima A, Tanimoto J, Nagayama K, Meno S (2009) Aerodynamic Parameters of Regular Arrays of Rectangular Blocks with Various Geometries. *Boundary-Layer Meteorology* 132(2):315–337, DOI 10.1007/s10546-009-9403-5
- Hanna SR, Brown MJ, Camelli FE, Chan ST, Coirier WJ, Hansen OR, Huber AH, Kim S, Reynolds RM (2006) Detailed Simulations of Atmospheric Flow and Dispersion in Downtown Manhattan: An Application of Five Computational Fluid Dynamics Models. *Bulletin of the American Meteorological Society* 87(12):1713–1726, DOI 10.1175/BAMS-87-12-1713
- Harman IN, Böhm M, Finnigan JJ, Hughes D (2016) Spatial Variability of the Flow and Turbulence Within a Model Canopy. *Boundary-Layer Meteorology* 160(3):375–396, DOI 10.1007/s10546-016-0150-0
- Harms F, Leitl B, Schatzmann M, Patnaik G (2011) Validating LES-based flow and dispersion models. *Journal of Wind Engineering and Industrial Aerodynamics* 99(4):289–295, DOI 10.1016/j.jweia.2011.01.007
- Hellsten A, Ketelsen K, Sühring M, Auvinen M, Maronga B, Knigge C, Barmas F, Tsegas G, Moussiopoulos N, Raasch S (2021) A nested multi-scale system implemented in the large-eddy simulation model PALM model system 6.0. *Geoscientific Model Development* 14(6):3185–3214, DOI 10.5194/gmd-14-3185-2021
- Kanani F, Träumner K, Ruck B, Raasch S (2014) What determines the differences found in forest edge flow between physical models and atmospheric measurements? – An LES study. *Meteorologische Zeitschrift* pp 33–49, DOI 10.1127/0941-2948/2014/0542
- Karttunen S, Kurppa M, Auvinen M, Hellsten A, Järvi L (2020) Large-eddy simulation of the optimal street-tree layout for pedestrian-level aerosol particle concentrations – A case study from a city-boulevard. *Atmospheric Environment: X* 6:100,073, DOI 10.1016/j.aeaoa.2020.100073
- Keskinen JP, Hellsten A (2025) Simulated data for the manuscript “ensembles in urban large eddy simulations with changing wind direction” by Keskinen and Hellsten. DOI 10.57707/FMI-B2SHARE.4EA51ED8864D465FB7D4C43B8BCE8972

- Keskinen JP, Vuorinen V, Larmi M (2011) Large Eddy Simulation of Flow over a Valve in a Simplified Cylinder Geometry. SAE Technical Paper pp 2011-01-0843
- Keskinen JP, Auvinen M, Hellsten A (in press) High-resolution case study of pollutant dispersion in an urban environment using large-eddy simulation. In: Air Pollution Modeling and its Application XXIX, Springer, Springer Proceedings in Complexity
- Khan B, Banzhaf S, Chan EC, Forkel R, Kanani-Sühring F, Ketelsen K, Kurppa M, Maronga B, Mauder M, Raasch S, Russo E, Schaap M, Sühring M (2021) Development of an atmospheric chemistry model coupled to the PALM model system 6.0: implementation and first applications. Geoscientific Model Development 14(2):1171-1193, DOI <https://doi.org/10.5194/gmd-14-1171-2021>
- Kurppa M, Roldin P, Strömberg J, Balling A, Karttunen S, Kuuluvainen H, Niemi JV, Pirjola L, Rönkkö T, Timonen H, Hellsten A, Järvi L (2020) Sensitivity of spatial aerosol particle distributions to the boundary conditions in the PALM model system 6.0. Geoscientific Model Development 13(11):5663-5685, DOI <https://doi.org/10.5194/gmd-13-5663-2020>
- Leonardi S, Castro IP (2010) Channel flow over large cube roughness: a direct numerical simulation study. Journal of Fluid Mechanics 651:519-539, DOI [10.1017/S002211200999423X](https://doi.org/10.1017/S002211200999423X)
- Letzel MO, Krane M, Raasch S (2008) High resolution urban large-eddy simulation studies from street canyon to neighbourhood scale. Atmospheric Environment 42(38):8770-8784, DOI [10.1016/j.atmosenv.2008.08.001](https://doi.org/10.1016/j.atmosenv.2008.08.001)
- Letzel MO, Helmke C, Ng E, An X, Lai A, Raasch S (2012) LES case study on pedestrian level ventilation in two neighbourhoods in Hong Kong. Meteorologische Zeitschrift pp 575-589, DOI [10.1127/0941-2948/2012/0356](https://doi.org/10.1127/0941-2948/2012/0356)
- Leutbecher M, Palmer TN (2008) Ensemble forecasting. Journal of Computational Physics 227(7):3515-3539, DOI [10.1016/j.jcp.2007.02.014](https://doi.org/10.1016/j.jcp.2007.02.014)
- Li W, Giometto MG (2023) Mean flow and turbulence in unsteady canopy layers. Journal of Fluid Mechanics 974:A33, DOI [10.1017/jfm.2023.801](https://doi.org/10.1017/jfm.2023.801)
- Lin D, Khan B, Katurji M, Bird L, Faria R, Revell LE (2021) WRF4PALM v1.0: a mesoscale dynamical driver for the microscale PALM model system 6.0. Geoscientific Model Development 14(5):2503-2524, DOI [10.5194/gmd-14-2503-2021](https://doi.org/10.5194/gmd-14-2503-2021)
- Maronga B, Raasch S (2013) Large-Eddy Simulations of Surface Heterogeneity Effects on the Convective Boundary Layer During the LITFASS-2003 Experiment. Boundary-Layer Meteorology 146:17-44, DOI [10.1007/s10546-012-9748-z](https://doi.org/10.1007/s10546-012-9748-z)

- Maronga B, Gryschka M, Heinze R, Hoffmann F, Kanani-Sühring F, Keck M, Ketelsen K, Letzel MO, Sühring M, Raasch S (2015) The Parallelized Large-Eddy Simulation Model (PALM) version 4.0 for atmospheric and oceanic flows: model formulation, recent developments, and future perspectives. *Geoscientific Model Development* 8(8):2515–2551, DOI 10.5194/gmd-8-2515-2015
- Maronga B, Banzhaf S, Burmeister C, Esch T, Forkel R, Fröhlich D, Fuka V, Gehrke KF, Geletič J, Giersch S, Gronemeier T, Groß G, Heldens W, Hellsten A, Hoffmann F, Inagaki A, Kadasch E, Kanani-Sühring F, Ketelsen K, Khan BA, Knigge C, Knoop H, Krč P, Kurppa M, Maamari H, Matzarakis A, Mauder M, Pallasch M, Pavlik D, Pfafferoth J, Resler J, Rissmann S, Russo E, Salim M, Schrempf M, Schwenkel J, Seckmeyer G, Schubert S, Sühring M, Tils Rv, Vollmer L, Ward S, Witha B, Wurps H, Zeidler J, Raasch S (2020) Overview of the PALM model system 6.0. *Geoscientific Model Development* 13(3):1335–1372, DOI 10.5194/gmd-13-1335-2020
- Munters W, Meneveau C, Meyers J (2016) Shifted periodic boundary conditions for simulations of wall-bounded turbulent flows. *Physics of Fluids* 28(2):025,112, DOI 10.1063/1.4941912
- Park SB, Baik JJ, Lee SH (2015) Impacts of Mesoscale Wind on Turbulent Flow and Ventilation in a Densely Built-up Urban Area. *Journal of Applied Meteorology and Climatology* 54(4):811–824, DOI 10.1175/JAMC-D-14-0044.1
- Patnaik G, Boris JP, Young TR, Grinstein FF (2007) Large Scale Urban Contaminant Transport Simulations With Miles. *Journal of Fluids Engineering* 129:1524, DOI 10.1115/1.2801368
- Patrinos AAN, Kistler AL (1977) A numerical study of the Chicago lake breeze. *Boundary-Layer Meteorology* 12:93–123, DOI 10.1007/BF00116400
- Pope SB (2000) *Turbulent Flows*. Cambridge University Press
- Sagaut P (2006) *Large eddy simulation for incompressible flows: an introduction*, 3rd edn. Scientific computation, Springer, Berlin ; New York
- Taylor KE (2001) Summarizing multiple aspects of model performance in a single diagram. *Journal of Geophysical Research: Atmospheres* 106:7183–7192, DOI 10.1029/2000JD900719
- Tseng YH, Meneveau C, Parlange MB (2006) Modeling Flow around Bluff Bodies and Predicting Urban Dispersion Using Large Eddy Simulation. *Environmental Science & Technology* 40(8):2653–2662, DOI 10.1021/es051708m
- Wicker LJ, Skamarock WC (2002) Time-Splitting Methods for Elastic Models Using Forward Time Schemes. *Monthly Weather Review* 130(8):2088–2097, DOI 10.1175/1520-0493(2002)130<textless2088:TSMFEM>textgreater2.0.CO;2

Williamson JH (1980) Low-storage Runge-Kutta Schemes. *Journal of Computational Physics* 35:48–56

Xie Z, Castro IP (2006) LES and RANS for Turbulent Flow over Arrays of Wall-Mounted Obstacles. *Flow, Turbulence and Combustion* 76(3), DOI 10.1007/s10494-006-9018-6